



Mid-infrared CO₂ sensor with blended absorption features for non-uniform laminar premixed flames

Zhenhai Wang¹ · Weitian Wang¹ · Liuhaio Ma² · Pengfei Fu³ · Wei Ren⁴ · Xing Chao¹

Received: 18 August 2021 / Accepted: 6 January 2022 / Published online: 25 January 2022
© The Author(s), under exclusive licence to Springer-Verlag GmbH Germany, part of Springer Nature 2022

Abstract

We develop a novel mid-infrared CO₂ absorption sensor exploiting spectrally blended features to characterize thermochemical non-uniformity of laminar premixed flames. A new algorithm for interpreting spectra with significantly blended features is proposed for single line-of-sight multi-transition absorption thermometry. A CO₂ sensor covering eight absorption transitions near 2378.0 cm⁻¹ is demonstrated in a laminar premixed CH₄/Air flame at an equivalence ratio of $\varphi = 1.0$. The average signal-to-noise ratio is 1293 with a measurement time of 1.0 s, and the estimated CO₂ detection limit is 42.8 ppm at 1543 K with 6 cm pathlength. Computational fluid dynamics (CFD) simulation with reduced GRI 1.2 mechanism is performed for comparison. Spatially resolved distributions are obtained with the laser absorption spectroscopy (LAS) measurements, combined with postulated distribution from CFD simulation. The LAS measurements agree with the CFD simulation, with a central-zone temperature difference of less than 1.1% and CO₂ concentration difference of less than 1.0%. Discrepancy is observed in the boundary layer region due to pronounced mixing with the ambient surroundings. The sensor developed provides a lead for general LAS sensor design (blended absorption features, ambient interference, or under optically thick conditions), and can serve for practical combustion sensing.

1 Introduction

Tunable diode laser absorption spectroscopy (TDLAS) has been proved to be a powerful species diagnostic tool over the past decades thanks to its capability of providing non-intrusive, highly sensitive and quantitative measurements of various gas properties [1–7]. A number of demonstrations harnessing a variety of laser sources [4, 5] and detection techniques [6, 7], show convincing potentials for sensing

targets from laboratory specialties to real-field combustion environments.

For a typical absorption-based measurement, the incident (I_0) and transmitted (I_t) intensities are related by the Beer–Lambert law. Quantitative measurement is achievable with tunable, narrow-linewidth lasers and accurate transition lineshape models at experimental conditions. Two most common schemes for TDLAS sensing include the direct absorption spectroscopy (DAS) and wavelength modulation spectroscopy (WMS). DAS is advantageous with isolated transitions of sufficient linestrength, but may be complicated by the requirement for correct evaluation of the non-absorbing baseline, as discussed in [8]. Conversely, WMS is the method of choice for applications in harsh environments with low absorbance, high pressure, or for absorbers with blended absorption features. Calibration-free WMS with first harmonic (1f) or residual amplitude modulation (RAM) normalization can actively account for the variation in I_0 caused by broadband transmission losses [9, 10].

On the other hand, TDLAS technique by nature recovers the line-of-sight (LOS)-averaged gas properties along the laser beam path. Several approaches have been adopted to retrieve spatially resolved distributions, including single-beam absorption thermometry with temperature probability

✉ Xing Chao
chaox6@tsinghua.edu.cn

¹ Key Laboratory for Thermal Science and Power Engineering of Ministry of Education, Department of Energy and Power Engineering, Center for Combustion Energy, Tsinghua University, Beijing 100084, China

² School of Automotive Engineering, Wuhan University of Technology, Wuhan, Hubei, China

³ School of Aerospace Engineering, Tsinghua University, Beijing 100084, China

⁴ Department of Mechanical and Automation Engineering, Shenzhen Research Institute, The Chinese University of Hong Kong, New Territories, Hong Kong SAR, China

distribution [11] or profile fitting strategy [12–15], and computed tomography with multiple laser beams [16, 17]. It is worth noting that with single-beam schemes only the temperature or concentration distribution can be retrieved instead of an arbitrary profile along the laser beam path. A singular-value-decomposition framework has been proposed by Rieker et al. to explore the theoretical limits to resolve temperature distributions with single-beam LOS absorption measurement [18, 19]. In this paper, we present a single-beam, mid-infrared (mid-IR) CO₂ absorption sensor exploiting several blended absorption features, for non-uniform temperature and concentration measurement of a laminar premixed flame. In particular, multi-line thermometry with profile-fitting strategy can serve as an alternative approach for two-dimensional reconstruction of an axisymmetric premixed flame, such as the flat flame of a McKenna burner. This differs from traditional two-dimensional tomography for an axisymmetric flame using Abel transform method, which can be realized by translating the laser beam or burner, aligning multiple parallel beams [20–23]. While two-dimensional tomography with translated- or parallel-beam schemes will increase the complexity of experimental systems, and considerable efforts are required to alleviate the ill-posedness of Abel inversion algorithms, the single LOS, multi-line method proposed here will be more advantageous for measurement scenarios with limited optical access or confined space.

Carbon dioxide is a principal product of hydrocarbon combustion, and extensive research has been dedicated to CO₂ sensing. Several of the commonly studied absorption bands of CO₂ include the 1.5 μm ($2\nu_1 + 2\nu_2 + \nu_3$), 2.0 μm ($\nu_1 + 2\nu_2 + \nu_3$), 2.7 μm ($\nu_1 + \nu_3$), and 4.2 μm (ν_3) rovibrational bands. Much of the earlier work utilized the weaker near-infrared (near-IR) combination bands near 1.5 μm [24], 2.0 μm [25] and the stronger vibrational band near 2.7 μm [26]. More recently, the maturity and commercialization of quantum cascade lasers (QCLs) and interband cascade lasers (ICLs) [4, 5] has enabled spectroscopic access to CO₂ sensing near 4.2 μm, where the fundamental band offers approximately 70 times stronger absorption than the vibrational band at 2.7 μm.

Previous works [12, 27, 28, 29, 30] (Wen et al. 2021) of CO₂ sensing near 4.2 μm have been demonstrated for sensitive measurements of flame temperature and CO₂ concentration [12, 15, 27–31]. Liu et al. presented a multi-line thermometry technique for sooting flames with an ICL probing the *R*-branch bandhead near 2397 cm⁻¹ [30]. Wen et al. further utilized the *R*-branch bandhead near 2397 cm⁻¹ to spatially and temporally resolve temperature measurements in counter-flow flames [15]. As shown in Fig. 1, this selection of lines features several unique benefits including absence of ambient CO₂ absorption (blue dashed line), high sensitivity at elevated temperatures (red solid line), and simultaneous

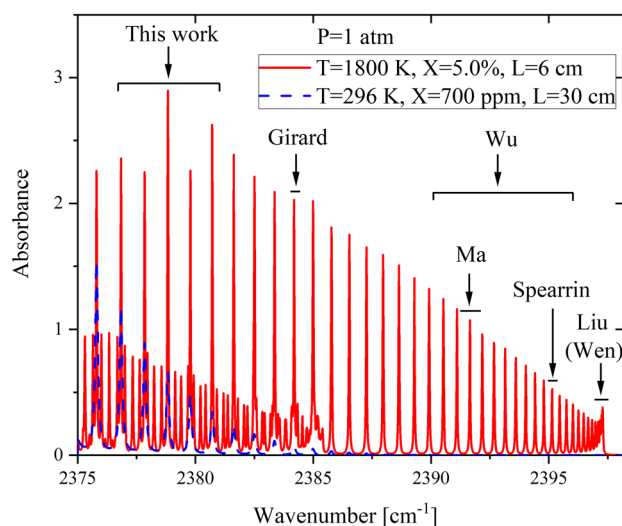


Fig. 1 Simulated absorbance profiles for CO₂ near 4.2 μm under ambient and typical combustion conditions

fitting of multiple transitions, making it suitable for combustion diagnostics. In contrast, the lower frequency transitions corresponding to lower *J* levels absorb significantly at a typical ambient CO₂ concentration of ~700 ppm and a pathlength of ~30 cm, leading to issues of self-interference. This poses considerable challenges for real-field combustion environments, where ambient CO₂ interference can be readily amplified by the much longer optical paths such that even optically thick conditions can be reached. Moreover, densely packed hot band lines at the low-frequency side of the 4.2 μm bandhead interfere with the ν_3 fundamental band at high temperatures, making the region harder to resolve under combustion conditions.

More generally, precise LAS sensor development imposes various design criteria, such as selection of well-isolated absorption lines, absence of blended hot bands, and ambient interference, which are nevertheless difficult to attain under the extreme conditions associated with combustion environments. Conditions including high temperature, pressure, and complicated composition, all render heavily blended rovibrational spectra. Moreover, novel broadband laser sources including frequency comb [32–36], Fourier-domain mode-locked (FDML) lasers [37], dispersed super-continuum sources [38], external cavity quantum cascade (ECQC) lasers [39, 40], etc., are being increasingly exploited thanks to their capability of providing broad spectral coverage for multi-parameter combustion sensing. Such sensor developments call for synergetic advancement of spectroscopic interpretation algorithms to extract quantitative information from the interblended absorption features.

In the context of DAS, an interference-feature baseline transform and background subtraction method (IFBTBS) has been proposed by the authors and the method has been

demonstrated to be effective for interpreting absorption spectra with interfering features in combustion environments [8]. Based on that, a new algorithm is presented in this work for interpreting absorption spectra with significantly blended features and further enables single-LOS, multi-transition, non-uniform absorption thermometry. A novel CO₂ absorption sensor near 2380 cm⁻¹ targeting a group of blended hot band lines and strongly interfering ambient lines is developed and demonstrated in a CH₄/Air premixed flame with spatial non-uniformity. Spatially resolved temperature and CO₂ concentration as a function of height-above-burner (HAB) at equivalence ratio is comprehensively investigated with the developed method. CFD simulation with reduced GRI 1.2 mechanism [41] is performed for comparison. In summary, the objectives of this work include:

1. To develop a novel mid-IR CO₂ absorption sensor near 2380 cm⁻¹ with relatively strong line strength, high temperature sensitivity, and free of interference from H₂O and CO.
2. To develop a new algorithm to interpret absorption spectra with significantly blended features in high-temperature combustion environments. This will open up new opportunity for general LAS sensor design with more flexible absorption line selection.
3. To investigate the thermochemical non-uniformity of a CH₄/Air premixed flame using LAS measurement and CFD simulation. This would further extend the applicability of single-LOS multi-transition absorption thermometry for combustion-related spectroscopic studies.

2 Fundamentals

2.1 Multi-line absorption spectroscopy under uniform conditions

The principle of laser absorption spectroscopy has been well documented [1–7], and here only relevant spectroscopic fundamentals are briefly outlined. The fractional transmission, τ_ν , defined as the ratio of the transmitted (I_t) and incident (I_0) intensities of light at frequency ν (cm⁻¹) through a uniform absorbing medium, is described by the Beer–Lambert relation:

$$\tau_\nu = \left(\frac{I_t}{I_0} \right) = \exp(-\alpha_\nu) = \exp[-S(T)P\chi_i\phi(\nu, T, P, \chi_i)L], \quad (1)$$

where α_ν denotes the spectral absorbance at frequency ν , $S(T)$ (cm⁻²·atm⁻¹) is the temperature-dependent line strength of the absorption transition, P (atm) the total gas pressure, χ_i the mole fraction of species i , ϕ (cm) the normalized lineshape function, and L (cm) the optical pathlength. The

temperature dependence of line strength S can be expressed as

$$S(T) = S(T_0) \frac{Q(T_0)}{Q(T)} \frac{T_0}{T} \exp \left[-\frac{hcE''}{k} \left(\frac{1}{T} - \frac{1}{T_0} \right) \right] \left[\frac{1 - \exp \left(-\frac{hc\nu_0}{kT} \right)}{1 - \exp \left(-\frac{hc\nu_0}{kT_0} \right)} \right], \quad (2)$$

where $S(T_0)$ is the line strength at reference temperature T_0 (typically 296 K), Q the partition function, E'' (cm⁻¹) the energy of the lower quantum state associated with the transition, and ν_0 the linecenter frequency. The constants h , c , and k are the Planck's constant, speed of light in vacuum, and Boltzmann's constant, respectively.

Two-line absorption thermometry is the most widely adopted technique to infer temperature from the ratio of integrated absorbance area A of two individual transitions. The temperature sensitivity of two-line absorption thermometry relies on the difference in the lower state energy E'' associated with the two absorption transitions, i.e., $\Delta E''$. As an extension to the two-line thermometry, Boltzmann plot method infers gas temperature and concentration based on information from multiple lines [42, 43]. This can be especially preferable for blended absorption features at high pressures or temperatures, as well as with broadband laser sources. Boltzmann plot equation can be obtained by reformulating Eqs. (1) and (2):

$$\ln \left[\frac{A_j}{S_j(T_0)} \right] = -\frac{hc}{k} \left(\frac{1}{T} - \frac{1}{T_0} \right) E''_j + \ln \left[\frac{Q_j(T_0)T_0}{Q_j(T)T} P\chi_i L \right] + \ln \left[\frac{1 - \exp \left(-\frac{hc\nu_{0j}}{kT} \right)}{1 - \exp \left(-\frac{hc\nu_{0j}}{kT_0} \right)} \right], \quad (3)$$

where subscript j denotes the j th transition.

The y -coordinate in a Boltzmann plot is the ratio of integrated absorbance area to absorption line strength at reference temperature T_0 . The x -coordinate is the lower state energy of the j th transition with j from 1 to n . The slope m is then solely a function of temperature. The last two terms in Eq. (3) constitute the y -intercept and can yield the species concentration with temperature determined. As illustrated in Fig. 2, the stimulated emission term (rightmost ratio in Eq. (2)) can be approximated by 1 for near-IR CO₂ absorption transition ($\nu_0 = 6359.97$ cm⁻¹) under typical combustion conditions (< 2500 K) [24]. However, it is worth noting that for the mid-IR absorption transition ($\nu_0 = 2377.8268$ cm⁻¹) used in this work, apparent deviation from such approximation requires the value to be computed exactly especially at high temperatures.

2.2 Non-uniform distribution with profile-fitting strategy

Multi-line thermometry with approximately 10 absorption transitions has been demonstrated to retrieve non-uniform

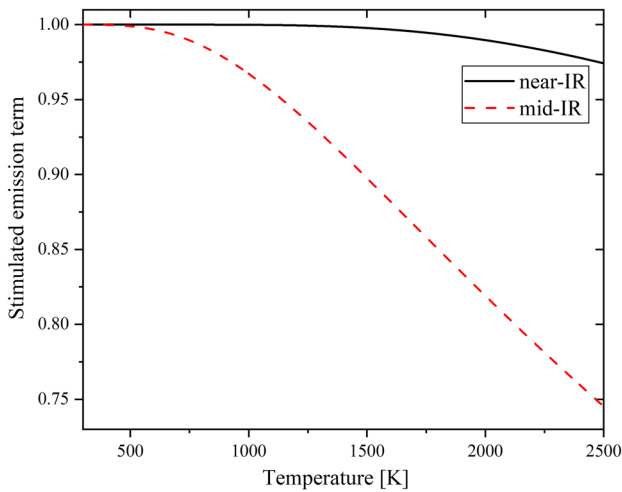


Fig. 2 Stimulated emission terms for the near-IR absorption transition ($\nu_0=6359.97 \text{ cm}^{-1}$) [24] and mid-IR absorption transition ($\nu_0=2377.8268 \text{ cm}^{-1}$) in this work from 300 to 2500 K, respectively

distribution along the laser beam path [44, 45]. Others have used single-LOS, multi-line thermometry to retrieve the maximum temperature in a two-section cell with a precision of 30 K [46, 47]. With additional absorption transitions, accuracy of the measured temperature or concentration distribution may be further improved. However, the theoretical limits of the spatially resolved temperature distributions with single-LOS absorption techniques still remain to be studied [18, 19].

Here we present a mid-IR CO₂ absorption sensor accessing a spectral range with several blended absorption features for non-uniform temperature and concentration measurement in laminar premixed flames. The sensor scheme utilizes single-LOS combined with postulated distribution function from validated CFD simulation. It has been demonstrated previously that a proper selection of multiple absorption lines along the single LOS is capable of reducing the non-uniform reconstruction uncertainty by 25% for high-temperature flames with profile-fitting strategy [14]. In this work, while the targeted region of blended CO₂ absorption features poses undesired challenges for conventional line-fitting routines and quantitative sensing, it also gives rise to promising potentials for non-uniform sensing in that multiple absorption transitions can be readily accessed with a single laser scan.

For non-uniform gas medium, the integrated absorption area can be expressed as

$$A_j = P \int_0^L X(x)S_j[T(x)]dx, \tag{4}$$

where $T(x)$ and $X(x)$ are the distributions of temperature and gas concentration along the optical path L , respectively.

A set of n equations can be established when n absorption transitions are measured simultaneously.

$$\begin{cases} A_1 = P \int_0^L X(x)S_1[T(x)]dx \\ A_2 = P \int_0^L X(x)S_2[T(x)]dx \\ \vdots \\ A_n = P \int_0^L X(x)S_n[T(x)]dx \end{cases}, \tag{5}$$

Such an equation set can be solved using the criteria of minimal residual:

$$\min_{T(x), X(x)} \left[\sum_{j=1}^n \left\{ \frac{P \int_0^L X(x)S_j[T(x)]dx - A_{\text{mea}}^j}{A_{\text{mea}}^j} \right\}^2 \right], \tag{6}$$

where A_{mea}^j is the measured integrated absorbance area of the j th transition. Optimization algorithms, such as genetic algorithm (GA) [16], simulated annealing (SA) algorithm [16], are efficient in searching for the optimal distributions of temperature and gas concentration.

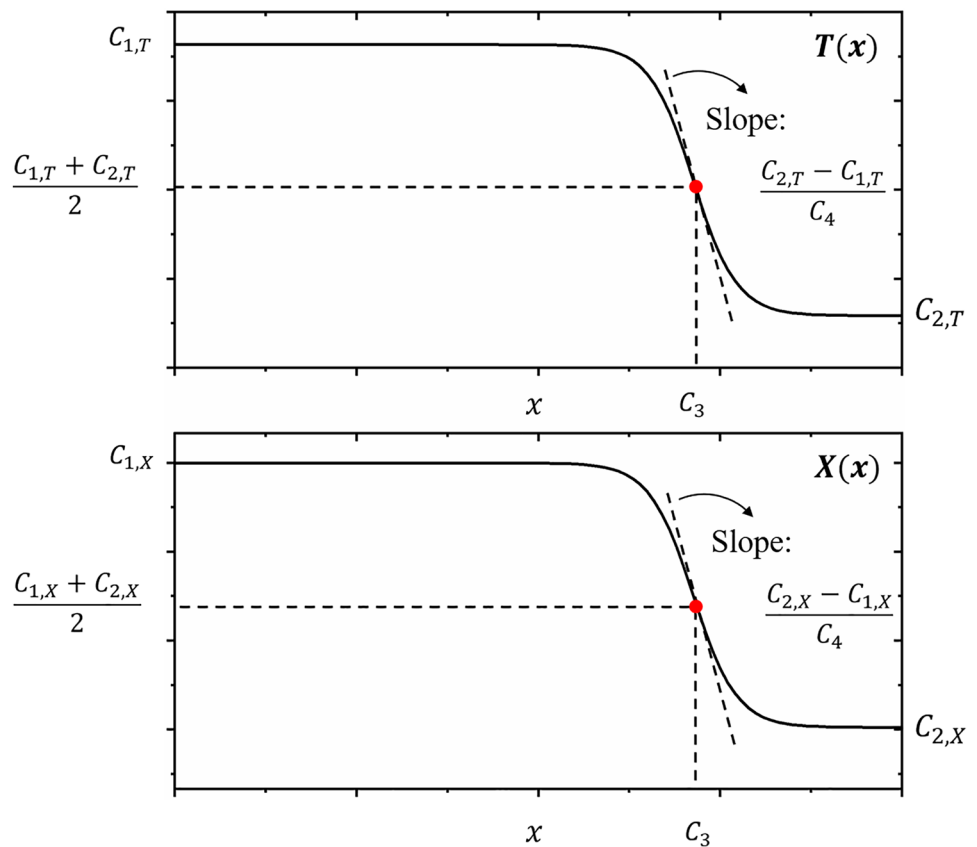
Stabilized laminar premixed flames from a McKenna burner have been widely investigated and its flame temperatures and species concentrations are assumed to be uniformly distributed along the radial direction [48]. However, thermochemical gradients in the boundary layer could lead to discrepancies between central zone and LOS-averaged temperature or species concentration measurements. Extensive researches have been dedicated to the thermal boundary layer effects on LAS measurement [12, 13, 49]. Postulated distribution with physical understanding and simulation studies can greatly mitigate the influence from the non-uniform characteristics along the laser beam path, hence, making it still a favorable model burner for both uniform and non-uniform diagnostic validation reference.

Over-simplified 2- T or trapezoid profile is not able to sufficiently characterize the non-uniform temperature and species concentration distribution for the laminar premixed flame investigated here [11]. Boltzmann profile-fitting strategy is used in [12] as described by Eqs. (7) and (8). More detailed illustrations of Boltzmann profile for temperature and species concentration distributions are shown in Fig. 3:

$$T(x) = C_{2,T} + \frac{C_{1,T} - C_{2,T}}{1 + \exp\left(\frac{x-C_3}{C_4}\right)}, \tag{7}$$

$$X(x) = C_{2,X} + \frac{C_{1,X} - C_{2,X}}{1 + \exp\left(\frac{x-C_3}{C_4}\right)}, \tag{8}$$

Fig. 3 Illustrations of Boltzmann profiles for temperature distribution (Upper panel) and species concentration (Lower panel). The red points are the radical position, where the temperature or species concentration is equal to $\frac{C_{1,T}+C_{2,T}}{2}$ or $\frac{C_{1,X}+C_{2,X}}{2}$



where $C_{1,T}$ and $C_{2,T}$ denote the temperature in the central flame zone and ambient surrounding, respectively. Similarly, $C_{1,X}$ and $C_{2,X}$ denote the species concentration in the central flame zone and ambient surrounding, respectively. C_3 is the radial position, where the temperature or species concentration is equal to $\frac{C_{1,T}+C_{2,T}}{2}$ or $\frac{C_{1,X}+C_{2,X}}{2}$. C_4 characterizes the gradient in the flame periphery or the boundary layer.

2.3 CFD simulation

CFD simulation is performed with reduced GRI 1.2 mechanism for comparison. Detailed geometry of the inner and outer burner structure (i.e., including the sintered stainless-steel porous media and the chamfers) are precisely specified in the computation domain, making the boundary conditions closer to the actual situation. The reactant flow (CH₄/Air) and N₂ co-flow are set as the velocity inlets based on the experimental conditions. In the computation, both the downstream and the surrounding environment boundaries are set as the pressure outlets. More detailed illustrations about CFD modeling can be found in our previous work [12, 13]. Boltzmann profile [described in Eqs. (7) and (8)] is determined based on non-uniform distributions obtained from CFD simulation. Table 1 shows typical Boltzmann-profile parameter values with the increase of HAB from CFD simulation at $\varphi = 1.0$. With validated CFD simulation, parameters

characterizing the Boltzmann profile in LAS experiments can be constrained to a limited range, enabling better recovery of the non-uniform distribution.

3 Sensor design and evaluation

3.1 Line selection and characterization

In this work, eight CO₂ absorption lines located between 2377.2 and 2379.0 cm⁻¹, including two lines ($R(44)$, $R(46)$) in the fundamental band and six lines [$R(73-78)$] in the hot band are chosen for CO₂ sensing. The spectroscopic parameters for the targeted CO₂ lines provided by HITEMP 2010 database [50] including wavenumber ν_0 (cm⁻¹), linestrength S (cm⁻²·atm⁻¹), lower state energy E'' (cm⁻¹), air-broadening coefficient γ_{air} (cm⁻¹·atm⁻¹), self-broadening coefficient γ_{self}

Table 1 Typical Boltzmann-profile parameter values with the increase of HAB from CFD simulation at $\varphi = 1.0$

HAB (mm)	$\alpha_{1,T}$ (K)	$\alpha_{1,X}$	α_3 (mm)	α_4 (mm)
5	1818	0.090	28.5	1.20
9	1804	0.0895	26.0	1.40
13	1795	0.0895	24.0	1.45

($\text{cm}^{-1} \cdot \text{atm}^{-1}$), and temperature dependence coefficient n_{air} for air-broadening coefficient are listed in Table 2. n_{self} is set to 0.75 to characterize the temperature dependence of self-broadening coefficient [51] for all transitions, since it is not included in the database.

A free-space distributed-feedback (DFB) interband-cascade laser (Nanoplus GmbH) operating near 4203.8 nm, with approximately 2.0 mW output power, serves as the monochromatic light source for the CO_2 sensor. The upper panel of Fig. 4 shows the wavelength tuning characteristics as a function of injection current and laser temperature measured with a wavelength meter (Bristol 771B). The absorption spectrum for 5% CO_2 at $T=1800$ K and $P=1$ atm with 6 cm pathlength is illustrated in the lower panel of Fig. 4. As shown, the eight transitions are closely spaced and can be readily accessed with a single laser scan. Ambient absorption of 700 ppm CO_2 is also shown in the lower panel of Fig. 4 for reference. The transitions are labelled with their relevant re-vibrational quantum notions, as $R(J'')$. Note that H_2O and CO produce no interference within this region and are not shown in Fig. 4. In a representative benchtop optical setup, ambient CO_2 interference cannot be neglected, making this portion of the CO_2 fundamental hot band challenging to use for many open-path studies.

As shown in the lower panel of Fig. 4, a weaker absorption transition $R(78)$ in the hot band almost coincides with the absorption transition $R(46)$ (with a line-center spacing of merely 0.0028 cm^{-1}), making the two lines difficult to reduce individually with multi-peak Voigt lineshape fitting. Instead, the sum of the two merged transitions can be treated effectively as a combined transition at $\nu_{0,w}$ but with a weighted linestrength $S_w(T)$ and lower state energy E_w'' . Wavenumber $\nu_{0,w}$ is set as $2378.8282 \text{ cm}^{-1}$, which is the average of the two transition centers of $R(78)$ and $R(46)$. The linestrength $S_w(T)$ of the resultant effective line can be expressed as Eq. (9), with reference temperature set at $T_0=296$ K.

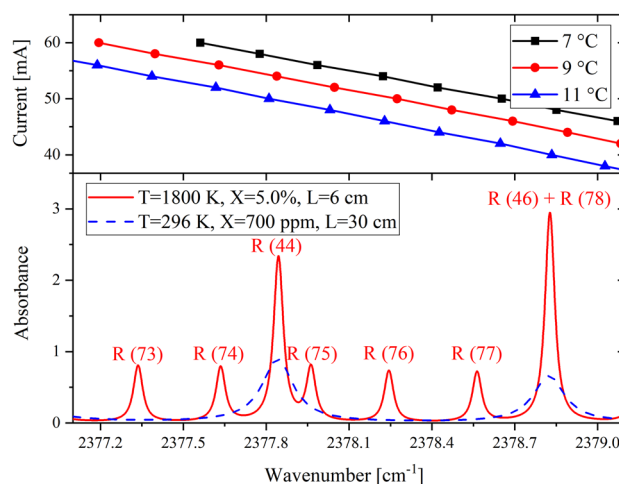


Fig. 4 Wavelength tuning characteristics of the CO_2 sensor at different operating temperatures (Upper panel) and Simulated absorbance profiles for CO_2 ambient and typical combustion environment (Lower panel)

$$S(T) = S(T_0) \frac{Q(T_0)}{Q(T)} \frac{T_0}{T} \exp \left[-\frac{hcE''}{k} \left(\frac{1}{T} - \frac{1}{T_0} \right) \right] \left[\frac{1 - \exp \left(-\frac{hc\nu_0}{kT} \right)}{1 - \exp \left(-\frac{hc\nu_0}{kT_0} \right)} \right] \tag{9}$$

It is worth noting that the linestrength $S_w(T)$ of the resultant effective line from 300 to 2800 K cannot be simply depicted with fixed weighted parameters ($S_w(T)$ and E_w'') due to the combination of two lines with different E'' . To accurately characterize the effective weighted multi-line parameters, the temperature dependence of the sum of linestrength of transitions $R(78)$ and $R(46)$ is fitted range-wise from 300 to 2800 K (Fig. 5): the linestrength curve is divided into five different sections and each least-square-fitted to yield one set of corresponding $S_w(T_0)$ ($\text{cm}^{-2} \cdot \text{atm}^{-1}$) and E_w'' (cm^{-1}), as listed in Table 3.

Table 2 Spectroscopic data for the CO_2 transitions of interest taken from the HITEMP 2010

ν_0	$S(296 \text{ K})$	$S(1800 \text{ K})$	E''	γ_{air}	γ_{self}	n_{air}	Transition
2377.3371	8.704E-4	0.1618	2773.6650	0.067	0.066	0.71	R(73)
2377.6355	6.546E-4	0.1559	2834.6538	0.067	0.066	0.71	R(74)
2377.8449	9.026	0.4946	772.1106	0.069	0.084	0.70	R(44)
2377.9633	5.083E-4	0.1513	2889.6282	0.067	0.065	0.71	R(75)
2378.2453	3.794E-4	0.1457	2952.3445	0.066	0.065	0.71	R(76)
2378.5643	2.926E-4	0.1413	3008.6794	0.066	0.065	0.71	R(77)
2378.8268	6.670	0.4877	843.0300	0.069	0.083	0.70	R(46)
2378.8296	2.165E-4	0.1358	3073.1271	0.066	0.065	0.71	R(78)

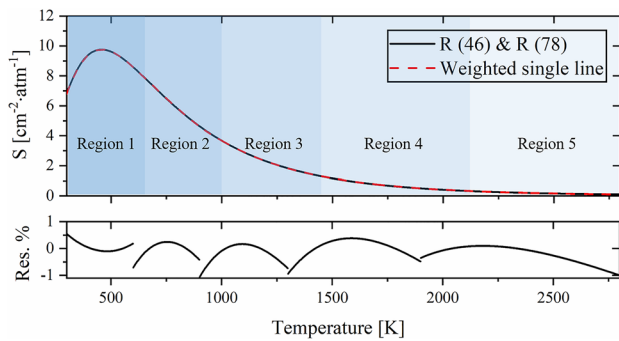


Fig. 5 Sum of linestrength of the two transitions $R(78)$ and $R(46)$

Table 3 Optimal $S_w(T_0)$ ($\text{cm}^{-2} \text{atm}^{-1}$) and E_w'' (cm^{-1}) for each range

Range	T (K)	$S_w(T_0)$	E_w''
1	300–600	6.63	847.8
2	601–900	5.89	894.1
3	901–1300	3.84	1023.0
4	1301–1900	1.68	1243.0
5	1901–2800	0.70	1455.0

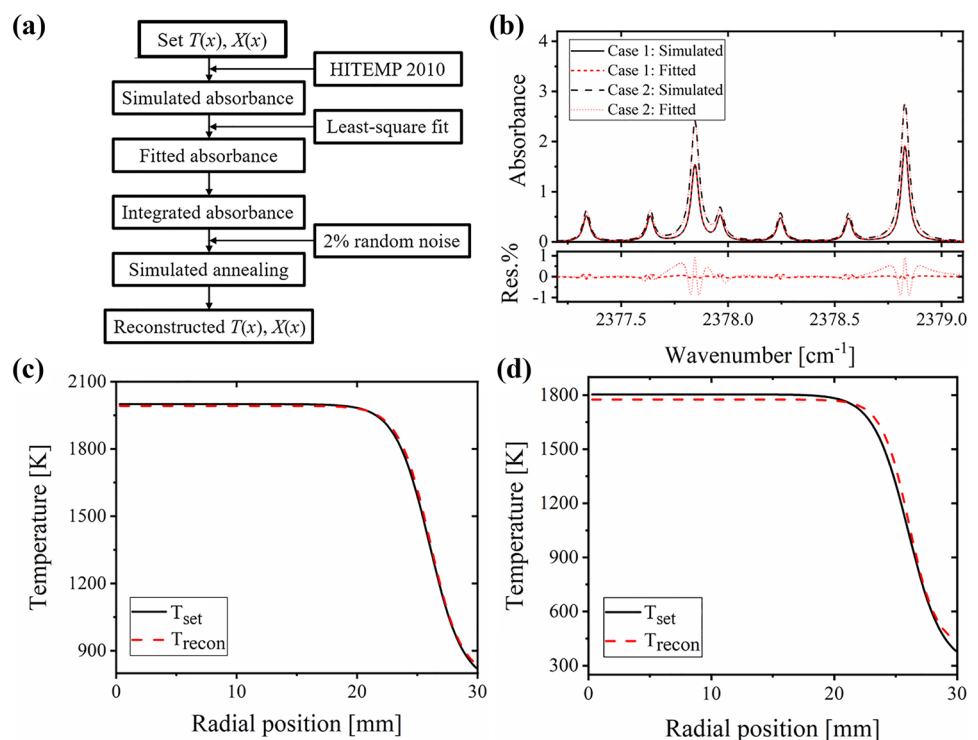
3.2 Evaluation of sensor performance on non-uniform absorption thermometry

It has been recognized that absorption line selection plays a critical role in LAS sensor design and performance. Previous

works have been mostly targeting the relatively simple case of sensing uniform temperature or concentration distributions with two or multiple absorption transitions. Wen et al. developed a CO₂ sensor utilizing the R-branch bandhead near 2397 cm^{-1} to spatially and temporally resolve temperature in counter-flow flames [15]. The CO₂ sensor captures the high temperature region well but fails to work at temperatures below 800 K due to the decreased temperature-sensitivity and weaker absorption at low temperatures. Instead of using the absorption transitions ($\Delta E''_{\text{max}} = 1892.4 \text{ cm}^{-1}$) in the R-branch bandhead [15], we extend the absorption line selection region to the low-frequency side of the $4.2 \mu\text{m}$ band ($\Delta E''_{\text{max}} = 2236.6 \text{ cm}^{-1}$). Here we evaluate the sensor performance under various non-uniform distribution conditions, i.e., different Boltzmann profiles given in Eqs. (7) and (8). Figure 6a shows the flowchart of the sensor performance evaluation process for non-uniform absorption thermometry. Initial $T(x)$ and $X(x)$ follow prior distributions obtained from CFD simulation. Two different cases are demonstrated: Case 1, $C_{1,T} = 2000\text{K}$, $C_{2,T} = 750\text{K}$; Case 2, $C_{1,T} = 1804\text{K}$, $C_{1,T} = 293\text{K}$. In both cases, $C_{1,X}$, $C_{2,X}$, C_3 , C_4 are set to mole fractions of 0.0895, 0.0008 (800 ppm), and lengths of 26.0 mm, 1.40 mm, respectively.

Simulated absorbance profiles can be calculated using the spectroscopic parameters from HITEMP 2010 database with initial non-uniform distributions [$T(x)$ and $X(x)$] determined along the optical pathlength. Path-integrated absorbance profile can then be simulated according to these distributions along the optical pathlength. Integrated absorbance

Fig. 6 **a** Flowchart of evaluation of sensor performance on non-uniform absorption thermometry, **b** simulated absorbance profiles, fitted Voigt profiles, and the relative fitting residuals, **c** and **d** Set and reconstructed average temperature distributions for the two cases, respectively



area for each absorption transitions can be deduced from non-linear least-square-fitted absorbance profiles. As illustrated in Fig. 6b, the Voigt fittings residuals are generally within 1.0% relative for both cases. As illustrated in [14], the relative error is mainly caused by the fact that the accumulated absorbance profile from simulation may not be accurately represented by a single Voigt profile. Furthermore, the relative residuals in case 1 is lower than case 2 due to stronger absorption from the six hot band lines at the higher temperatures in the boundary layer of case 1. Simulated annealing algorithm is utilized to obtain the optimal temperature and concentration distributions, i.e., to find the optimal parameters including $C_{1,T}$, $C_{2,T}$, $C_{1,X}$, $C_{2,X}$, C_3 , C_4 . The search domain for $C_{1,T}$ is limited to ± 200 K and for other five parameters from 0 to infinity. The iterative reconstruction process of non-uniform distributions is repeated for 1000 cases with 2% random noises incorporated in the fitted integrated absorbance area.

Figure 6c, d shows the set and reconstructed average temperature distributions for the two cases, respectively. For case 1, the sensor captures the temperature distribution from 800 to 2000 K well and the maximum deviation between the set and reconstructed distributions is 30 K in the boundary layer. The average central temperature difference for case 2 is found to be within 25 K ($< 1.4\%$) and notable disparities (~ 90 K) are observed in the boundary layer. This is due to the weak absorption of the selected lines at lower temperatures. Compared to the absorption lines at the R -branch bandhead near 2397 cm^{-1} , the selected lines at the low-frequency side in this work have higher temperature sensitivity at low temperature, making it suitable to capture the temperature transition in the boundary layer regions. Hence the advantage of using the absorption lines at the low-frequency side of the $4.2\text{ }\mu\text{m}$ band compared with the R -branch bandhead is verified for prospective applications in practical combustion environments.

4 IFBTBS method for ambient interference and blended absorption features

As shown in Fig. 4, ambient CO_2 interference cannot be neglected, so nitrogen or inert gas purging of the exposed optical path would be desired to eliminate the interference. However, as in many practical cases, the highly limited optical access or difficulty in using pitch or catch fibers for accessing the measurement spot (e.g., with mid-IR laser), as well as real-field conditions requiring long open paths, make purging of the entire optical path difficult or completely impractical. This makes the multi-line absorption scheme potentially attractive, as the targeted combustion and ambient section conditions along the laser beam path can be deduced directly from the LOS path-integrated measurements.

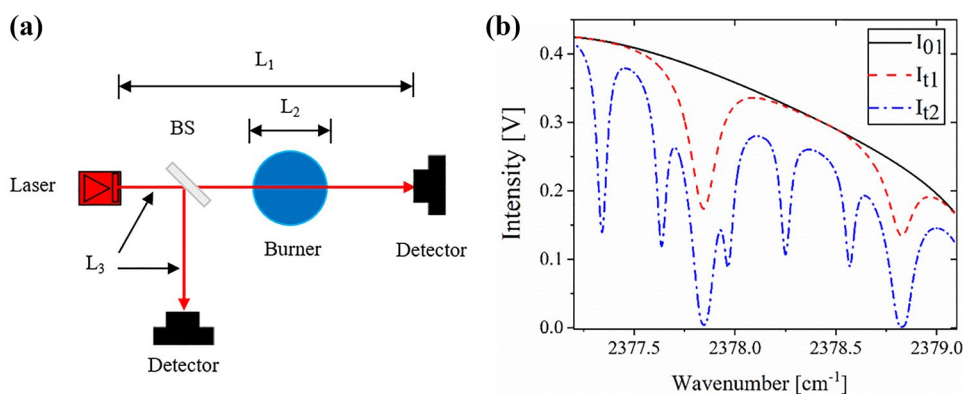
Figure 7a shows a simplified schematic of the CO_2 LAS experimental setup to define terms and symbols. The laser beam is split into two equal intensity paths (50:50) using a beam splitter, with one propagating through the flat-flame burner (diameter $L_2 = 6$ cm) and the other serving as the reference to eliminate ambient interference by carefully adjusting the optical length to $L_3 = L_1 - L_2$. Identical photodetectors are used in two paths and the values of L_1 and L_3 are set as 28 cm, 22 cm in the experiments, respectively. One major complication is that with ambient absorbance being strong in this band the accumulated absorption readily saturates and reaches optically thick conditions. Treatment for this problem will be detailed in Sect. 5.3 in the following. The Beer–Lambert relations can be expressed as follows:

$$I_{t1} = I_{01} \exp(-\alpha_{L_1}) = I_{01} \exp(-\alpha_{L_2} - \alpha_{L_3}), \quad (10)$$

$$I_{t2} = I_{02} \exp(-\alpha'_{L_1}) = I_{01} \exp(-\alpha'_{L_2} - \alpha_{L_3}), \quad (11)$$

$$I_{t3} = I_{03} \exp(-\alpha_{L_3}), \quad (12)$$

Fig. 7 **a** Schematic diagram of CO_2 LAS experimental setup. BS, beam splitter, **b** Typical measured CO_2 absorption raw signals at 5 mm height of a CH_4/Air flame ($\varphi = 1.0$)



where I_{01} and I_{02} denote the incident non-absorbing laser intensities of the measurement path under room and flame temperature conditions, respectively. I_{03} is the incident non-absorbing intensity of the reference path at room temperature. Similarly, I_{11} and I_{12} are the transmitted laser intensities under room and flame temperature conditions, and I_{13} is the transmitted laser intensity of the reference path. α_{L_1} , α_{L_2} and α_{L_3} are the ambient CO₂ absorbance with optical pathlength L_1 , L_2 and L_3 , respectively. α'_{L_2} is the CO₂ absorbance in high-temperature flame with an optical pathlength of L_2 .

Figure 7b shows typical measured raw signals in a flame experiment including incident intensity I_{01} and transmitted intensities I_{11} and I_{12} at an equivalence ratio of $\phi = 1.0$. I_{01} can be directly obtained through polynomial baseline fitting of non-absorbing portions of I_{11} with sufficiently isolated absorption features at room temperature. On the other hand, as can be seen in Fig. 7b, in the case of severe blending from the hot band absorption features at high-temperatures, it is impossible to find sufficient non-absorbing spectral regions in the measured transmitted signal I_{12} for the corresponding baseline fitting.

In our previous work [8], it has been demonstrated that I_{01} under room temperature condition contains sufficient information on laser tuning and detection characteristics that can be used to emulate the incident non-absorbing intensity I_{02} under flame temperature conditions. More specifically, I_{01} can be scaled (for attenuation) and shifted (for background offset correction) to closely match the measured transmitted signal I_{12} . The empirical baselines of I_{02} are obtained through non-absorbing baseline transform of I_{01} , which further serve to reduce the measured transmitted signal I_{12} to the absorbance profile. Background adjustment is conducted through orthogonal polynomial expansion and subtraction of the first three components and modified absorbance profile can then be obtained. More detailed illustration about the IFBTBS method can be found in [8]. Here, based on the previously developed IFBTBS method, a new algorithm is proposed for sensitive detection of CO₂ with blended features in combustion gases and ambient gas absorption interference. Then integrated absorbance area for each absorption transition can be obtained from the best-fitted modified absorbance profile with a Voigt lineshape. Boltzmann plot method follows to deduce the LOS-averaged temperature and CO₂ concentration with integrated absorbance area determined. Furthermore, non-uniform distribution of temperature or CO₂ concentration can be recovered with prior information obtained from validated CFD simulation.

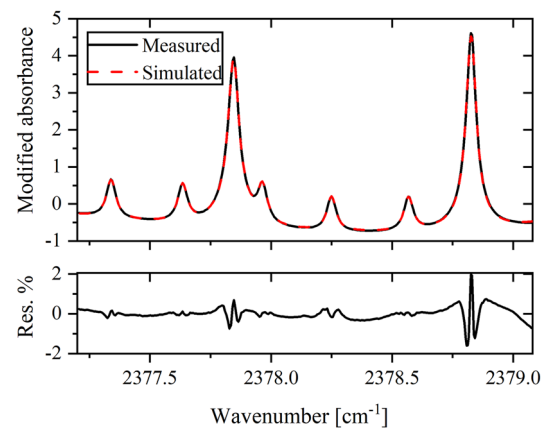


Fig. 8 Typical modified absorbance profile of CO₂ at $\phi = 1.0$ and HAB = 9 mm

5 Experimental results and discussion

5.1 LAS optical configuration

The mid-IR CO₂ sensor using blended absorption features is demonstrated in premixed CH₄/Air laminar flat-flame burner. As illustrated in Fig. 7a, the incident beam from the DFB laser (4203.8 nm) is split with a CaF₂ beam splitter (Thorlabs, BSW511) to provide the measurement path (through the flat-flame burner) and the reference path (through ambient CO₂). A collinear visible laser is used to assist the alignment of the mid-IR laser above the burner surface with two irises (~1 mm diameter open aperture). Each laser beam is spectrally filtered with a narrow bandpass filter (Spectrogon, NB-4230–64 nm), and then focused onto the photodetector (Vigo System, PVI-3TE-6). The experiment is conducted at various HAB (5 mm, 9 mm, 13 mm) with a total air flow rate of 14.4 L/min ($\phi = 1.0$). The flow rate of annular shroud N₂ co-flow is 10 L/min. A 100 Hz sawtooth function provided by a software-controlled function generator is used to access the eight target absorption lines with a single scan. A Ge-etalon (0.0164 cm⁻¹ free-spectral-range) is utilized to calibrate the relative wavelength tuning characteristics.

5.2 Flat-flame measurement results and discussion under uniform conditions

Based on the previously developed IFBTBS method, a typical modified absorbance profile of both measured and fitted CO₂ spectra after removal of ambient CO₂ interference from the reference path is shown in the upper panel of Fig. 8. The measured absorbance profile results from 100 averages of consecutive transmitted intensities at HAB = 9 mm, each with an acquisition time of 10 ms. The relative fitting residuals in the lower panel of Fig. 8 are all below 2.0% within the

fitted spectral range. Here we define the signal-to-noise ratio (SNR) as the peak modified absorbance value divided by the standard deviation of the relative residuals in Fig. 8. The SNR is 1293 at a measurement time of 1.0 s. The measured integrated absorbance area $A_{\text{mea},j} (j = 1, 2, \dots, 7)$ for each transition can be derived from Fig. 8. The uncertainties of the inferred integrated area are estimated to be 0.28% and 1.4% at 95% confidence interval (CI) with non-linear least-square fit for the two lines in the fundamental band and five lines in the hot band, respectively.

To further investigate the advantage of multi-line thermometry over conventional two-line thermometry under uniform conditions, two different cases are demonstrated: Case 1, absorption thermometry with 8 lines; Case 2, absorption thermometry with a representative selection of 2 lines ($R(44): E_w'' = 772.1 \text{ cm}^{-1}$ and $R(77): E_w'' = 3008.7 \text{ cm}^{-1}$). Note that the eight lines in Case 1 refer to the full set of CO_2 absorption transitions with two coincident lines $R(78)$ and $R(46)$, as listed in Table 2. In both cases, the maximum differences in the lower-state energy E'' associated with the selected absorption transitions are the same. LOS-averaged temperature and CO_2 concentration are deduced by multi-line or two-line Boltzmann plot method with the measured integrated absorbance area for each transition derived from Fig. 8.

Take multi-line Boltzmann plot in Case 1 as an example, the best linear fit in the upper panel of Fig. 9a yields $T = 1543 \text{ K}$, $X_{\text{CO}_2} = 5.54\%$ at $\text{HAB} = 9 \text{ mm}$ and the black point at $E_w'' = 1243.0 \text{ cm}^{-1}$ denotes the weighted line of $R(78)$ and $R(46)$, as reported in Table 3. Independent sources of uncertainty associated with multi-line Boltzmann plot include uncertainty of the reference temperature linestrength ($\sim 2.0\%$ [29]), uncertainty of the integrated area (0.28% or 1.4% at 95% CI), and uncertainty of ambient CO_2 absorption removal from the reference path ($\sim 2.0\%$). These accumulate to a combined uncertainty of LOS-averaged temperature of

24.0 K and absolute CO_2 concentration of 0.21% in Case 1, according to the propagation of uncertainty in the least-squares fitting of a straight line [52]. The detection limit is defined as the noise-equivalent ppm CO_2 level at a given pressure and pathlength, and thus estimated to be 42.8 ppm at $T = 1543 \text{ K}$, $X_{\text{CO}_2} = 5.54\%$. Similarly, in Case 2, the best linear fit in the upper panel of Fig. 9b gives $T = 1558 \text{ K}$, $X_{\text{CO}_2} = 5.76\%$ at $\text{HAB} = 9 \text{ mm}$, with an uncertainty of LOS-averaged temperature to 36.7 K and absolute CO_2 concentration of 0.33%.

Fitted integrated absorbance area $A_{\text{fit},j}^{\text{Uni}} (j = 1, 2, \dots, 7)$ for each transition can be determined using the linear-fitted ordinate values determined by multi-line or two-line Boltzmann plot method under uniform conditions. The relative residual, $\epsilon_{A,j}^{\text{Uni}}$, in the integrated absorbance area for each transition in two cases, can be defined as:

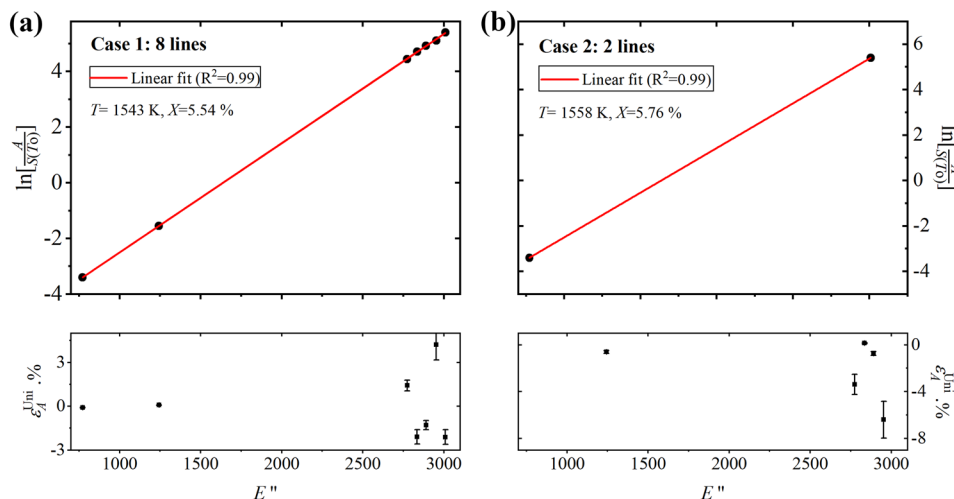
$$\epsilon_{A,j}^{\text{Uni}} = \frac{A_{\text{mea},j} - A_{\text{fit},j}^{\text{Uni}}}{A_{\text{mea},j}}, j = 1, 2, \dots, 7, \tag{13}$$

The sum of squared relative residual, $\epsilon_{A,\text{sum}}^{\text{Uni}}$, is expressed as Eq. (14) and this is consistent with the criteria in non-uniform reconstruction, as described in Eq. (6):

$$\epsilon_{A,\text{sum}}^{\text{Uni}} = \sum_{j=1}^7 \left| \epsilon_{A,j}^{\text{Uni}} \right|^2 \tag{14}$$

The lower panel of Fig. 9a shows the value of $\epsilon_{A,j}^{\text{Uni}}$ in Case 1. Uncertainty of $\epsilon_{A,j}^{\text{Uni}}$ for each transition is estimated from the evaluation of both $A_{\text{mea},j}$ and $A_{\text{fit},j}^{\text{Uni}}$, and magnified 10 times for better visualization. It is obvious that the relative residuals of the two lines ($E_w'' = 772.1 \text{ cm}^{-1}, 1243.0 \text{ cm}^{-1}$) in the fundamental band are significantly lower than those of the five lines in the hot bands. It can be mathematically interpreted that the two relatively discrete points at low E_w'' values could dominate in linear least-squares regression

Fig. 9 **a** Multi-line Boltzmann plot (Upper panel) for each transition (black point) and linear fit (red solid line), relative residual in the integrated absorbance area (lower panel), **b** two-line Boltzmann plot (upper panel) for each transition (black point) and linear fit (red solid line), relative residuals of the other six transitions in the integrated absorbance area (Lower panel)



compared to the five tightly spaced points at large E_w'' values. The mean absolute residual in percent for 8 lines is 1.61% and sum of squared relative residual is 30.2×10^{-4} in Case 1. In Case 2, the relative residuals of the 2 lines ($R(44)$: $E_w'' = 772.1 \text{ cm}^{-1}$ and $R(77)$: $E_w'' = 3008.7 \text{ cm}^{-1}$) are zero in two-line linear fit and not shown in the lower panel of Fig. 9b. The mean absolute residual in percent for other 5 lines is 2.25% and sum of squared relative residual is 53.2×10^{-4} in Case 2. Overall, under uniform conditions, multi-line thermometry (Case 1) outperforms conventional two-line thermometry (Case 2) in both measured uncertainty and relative residual. More detailed comparisons between two cases at HAB = 5 mm, 13 mm are summarized in Table 4 (see Sect. 5.3) and will be discussed later.

5.3 Flat-flame measurement results and discussion in non-uniform reconstructions

Non-uniform absorption thermometry with Boltzmann profile-fitting strategy is demonstrated for temperature and CO₂ concentration reconstructions of the studied laminar premixed flame. Under uniform conditions, ambient CO₂ with optical pathlength L_3 (22 cm) is assumed to be uniform and subtracted through the reference path. However, for non-uniform reconstruction, width of the flame region including the thermal boundary layer is extended to 8 cm, which has been verified in our previous studies [12, 13]. Correspondingly, 20 cm optical pathlength in the ambient surrounding is assumed to be uniform and subtracted through the reference path before non-uniform reconstruction.

As illustrated in Sect. 3.2, SA algorithm is utilized to obtain the optimal temperature and concentration distributions, i.e., to find the optimal Boltzmann-profile parameters including $C_{1,T}$, $C_{2,T}$, $C_{1,X}$, $C_{2,X}$, C_3 , C_4 . It is worth noting that the performance of SA algorithm strongly depends on a

number of critical factors including the starting temperature T_{st} , cooling schedule, initial parameter values and the search domain for the parameters, i.e., lower and upper bounds. Previous works showed that SA algorithm with a sufficiently high T_{st} and a slow cooling schedule would be preferred to ensure a satisfactory solution [53, 54]. To further decrease the complexity of the non-uniform iterative reconstructions, $C_{2,T}$ is set to 293 K, while $C_{2,X}$ is estimated to be 780 ppm. This has been repeatedly verified using LAS technique under room temperature conditions with the same experimental optical configuration before the flat-flame experiments, and the standard deviation of ambient CO₂ measurement is 8.0 ppm in 1.0 s. It is worth emphasizing that CO₂ is more stable than H₂O in the ambient surroundings, making the developed mid-IR CO₂ sensor more accurate in ambient background subtraction than the previously reported near-IR H₂O sensor [11]. CFD simulation is performed for comparison with the non-uniform characterization of the LAS measurement. As has been discussed in Sect. 2, parameters involved in multi-line Boltzmann profile-fitting strategies can be constrained to a reasonably limited range from CFD simulation. However, as a probabilistic and metaheuristic method, SA algorithm can be easily stuck in the local minima or lower/upper bounds with an excessively limited search domain for the parameters, i.e., over-saturated prior information. Moreover, such prior information is not always available in practical combustion environments. Here, in this work, the search domain for other four parameters including $C_{1,T}$, $C_{1,X}$, C_3 , C_4 , are within $\pm 50\%$ of typical Boltzmann-profile parameter values shown in Table 1. Such broad search domain has been verified to ensure robust and repeatable reconstructions for both cases. The initial values for other four Boltzmann-profile parameters are randomly generated in the search domain at each iteration.

Table 4 Absolute relative residuals expressed in percentiles for each transition, $|\epsilon_A^{\text{Uni}}|$ and $|\epsilon_A^{\text{Non-uni}}|$, as well as $\epsilon_{A,\text{sum}} (\times 10^{-4})$ at various HABs

HAB (mm)	Cond	$R(73)$	$R(74)$	$R(44)$	$R(75)$	$R(76)$	$R(77)$	$R(46), R(78)$	$\epsilon_{A,\text{sum}} (\times 10^{-4})$
5	Uniform, 8 lines	1.22	1.82	0.21	0.38	3.58	2.36	0.33	23.50
	Uniform, 2 lines	3.39	0.35	—*	1.89	6.01	—*	0.01	51.35
	Non-uniform, 8 lines	1.99	0.60	6.54	1.75	4.41	2.36	1.51	77.41
	Non-uniform, 2 lines	0.51	2.64	3.10	4.91	2.20	5.50	1.75	79.15
9	Uniform, 8 lines	1.42	2.09	0.09	1.28	4.21	2.10	0.09	30.19
	Uniform, 2 lines	3.38	0.14	—*	0.73	6.39	—*	0.60	53.22
	Non-uniform, 8 lines	1.99	1.62	4.26	0.85	7.40	1.39	1.88	85.63
	Non-uniform, 2 lines	2.92	6.37	1.63	5.65	2.18	3.56	1.34	102.9
13	Uniform, 8 lines	1.83	2.34	0.12	2.10	4.71	1.93	0.14	39.18
	Uniform, 2 lines	3.63	0.57	—*	0.27	6.72	—*	0.64	59.18
	Non-uniform, 8 lines	0.01	4.10	1.80	3.80	5.75	0.35	0.47	68.00
	Non-uniform, 2 lines	2.21	6.24	0.33	5.94	3.39	2.60	2.13	102.0

—*Relative residuals of two lines ($R(44)$ and $R(77)$) are zero in two-line linear fit and not shown in Table 4

For each set of six Boltzmann-profile parameters, temperature and concentration distributions can be calculated. The corresponding $S_w(T_0)$, E_w'' of the resultant effective line can then be determined at each discrete temperature value according to Table 3. Same non-uniform reconstruction process is repeated for the two cases in Sect. 5.2 to further investigate the sensor performance with multi-line and two-line absorption thermometry. The starting temperature in SA algorithm is set to 1000 K, followed by a Boltzmann-distribution cooling schedule in both cases [53]. Figure 10 presents the measured and simulated radial distributions of temperature and CO₂ concentrations at HAB = 9 mm in Case 1 and 2. Uncertainty of CFD simulation result is determined by introducing 2% variation in the inlet boundary conditions of the flat-flame burner. Two major sources of error can contribute to the aggregated uncertainty of non-uniform LAS measurement for two cases: lineshape fitting error in obtaining the measured integrated absorbance, which has been estimated at 95% CI from the non-linear least-square fit of the integrated area for each absorption line, and uncertainty of high-temperature spectroscopic parameter, $S(T)$, which is estimated to be about 5%. The iterative reconstruction process of non-uniform distributions is repeated for 1000 cases with random noises of the given level incorporated in the integrated area and $S(T)$. The uncertainties of non-uniform temperature and CO₂ concentration in LAS measurements for two cases are estimated from the 1000 realizations.

As directly observed from Fig. 10, the flame temperature and CO₂ concentration by LAS measurement in the central uniform region for Case 1 and 2 is in excellent agreement with the CFD simulation at HAB = 9 mm. Certain degree of discrepancy between LAS measurement and CFD simulation is observed in the thermal boundary layer region due to pronounced mixing with the ambient surroundings, and such deviation within the boundary layer region becomes more significant in Case 2 than that in Case 1. With multiple absorption lines in the non-uniform reconstruction, the radial position of boundary layer can be captured more accurately than that with only two lines selected at HAB = 9 mm. It indicates that using the full set of selected CO₂ absorption

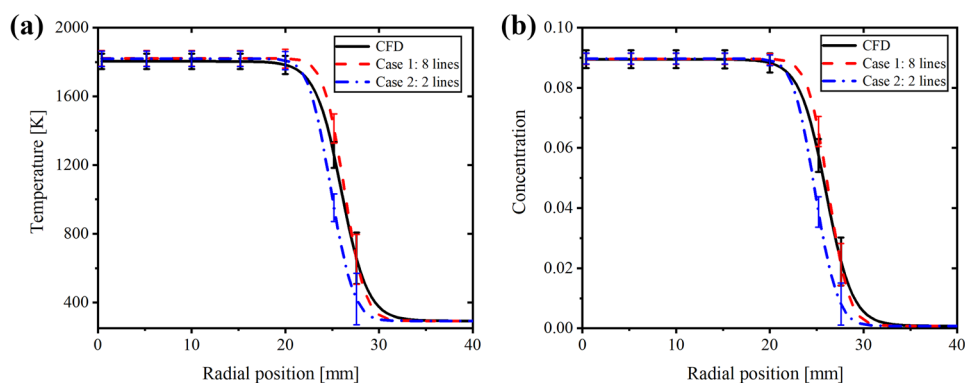
lines exhibits superior performance in non-uniform reconstruction over conventional two-line absorption thermometry. The same performance holds for the non-uniform reconstruction at HAB = 5 mm, 13 mm.

Similarly, fitted integrated absorbance area $A_{\text{fit},j}^{\text{Non-uni}}$ ($j = 1, 2, \dots, 7$) for each transition can be determined from optimal non-uniform reconstruction conditions. The relative residual, $\epsilon_A^{\text{Non-uni}}$, in the integrated absorbance area for each transition, and the sum of squared relative residual, $\epsilon_{A,\text{sum}}^{\text{Non-uni}}$, are defined in the same way as in Eqs. (13) and (14), respectively. The absolute relative residuals, $|\epsilon_A^{\text{Uni}}|$ and $|\epsilon_A^{\text{Non-uni}}|$ for each transition, as well as $\epsilon_{A,\text{sum}}$ at various HAB (5 mm, 9 mm, and 13 mm) are summarized in Table 4.

As illustrated in Table 4, several key conclusions are worth highlighting:

1. Under uniform conditions: two lines ($E_w'' = 772.1 \text{ cm}^{-1}$, 1243.0 cm^{-1}) in the fundamental band present lower relative residuals than those of other five lines in the hot bands at HAB = 5 mm, 13 mm in Case 1. This is consistent with the results at HAB = 9 mm as discussed in Sect. 5.2. The sums of squared relative residual in Case 1 (8 lines) are lower than those in Case 2 (2 lines) at various HAB in uniform conditions.
2. For non-uniform reconstructions: the residual distribution for CO₂ transitions in the two cases becomes complex and irregular. As shown under uniform conditions, the sums of squared relative residual in Case 1 (8 lines) are lower than those in Case 2 (2 lines) at various HAB in non-uniform reconstructions.
3. Non-uniform reconstruction results present slightly larger residuals in Case 1 and 2 compared to those in uniform conditions at various HAB. The reason could lie in two aspects: increased uncertainty of high-temperature spectroscopic parameters, e.g., $S(T)$ and line profiles, can impair accurately characterization of the non-uniform distribution; on the other hand, due to limited tunability of a single DFB laser, only two groups of transitions with E_w'' centered around 770 cm^{-1} and

Fig. 10 Radial temperature (a) and concentrations (b) distribution at HAB = 9 mm. Black solid lines: CFD simulation; Red dash lines: Case 1, 8 lines; Blue dash dot lines: Case 2, 2 lines



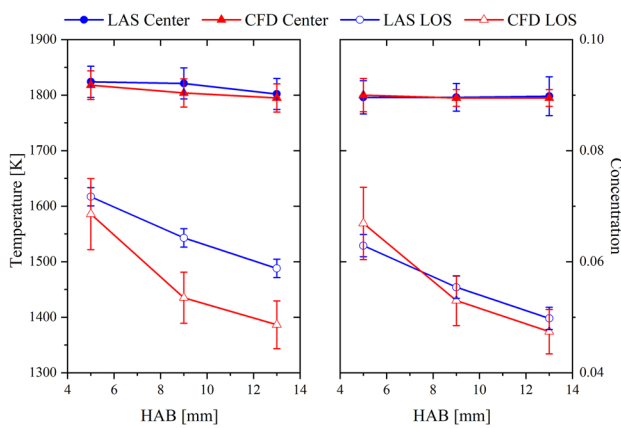


Fig. 11 Central and LOS-averaged flame temperature (left panel) and CO₂ concentration (right panel) along the HAB at $\varphi = 1.0$ from LAS measurement (Case 1) and CFD simulation

2800 cm⁻¹ can be accessed. The performance in non-uniform reconstruction with the selected group of lines is difficult to be further improved significantly.

In summary, it is verified that multi-line thermometry shows its advantages over conventional two-line thermometry under uniform and non-uniform conditions. It is also proved that with more absorption features and broader E_w'' span, the performance of non-uniform reconstruction will improve. However, it is yet still an open question to determine optimal absorption line selection in non-uniform reconstruction problems and more detailed discussions could be found in Ref. [18] and [19].

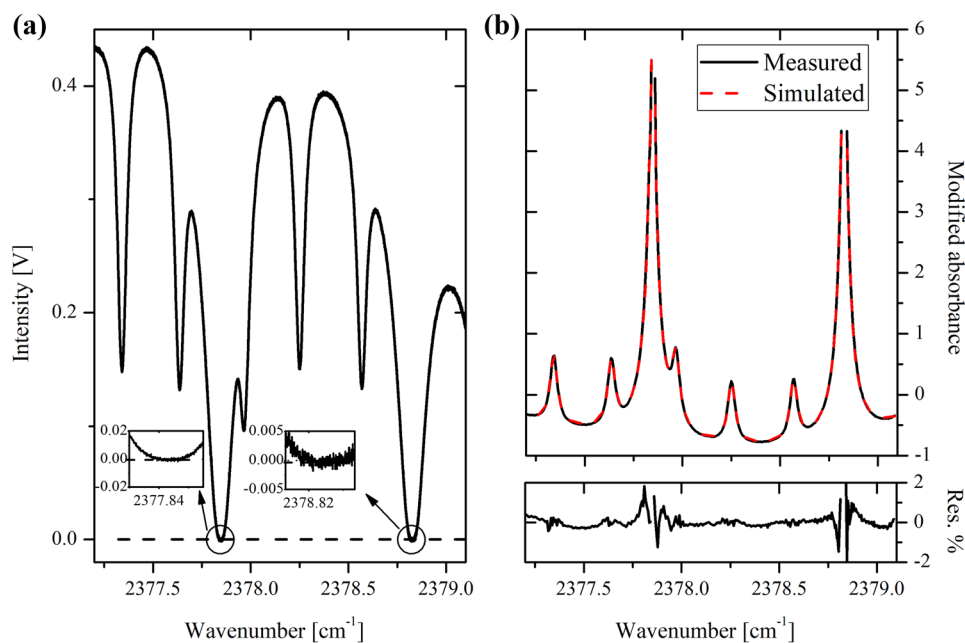
For more illustrative quantitative comparison of the results, Fig. 11 shows (with closed symbols) the axial flame temperature and CO₂ concentration at $\varphi = 1.0$ in LAS measurement for Case 1. The central flame temperature and CO₂ concentration of CFD simulation also generally agree with LAS measurement at HAB = 5 mm, 13 mm. The flame temperature tends to decrease with the increase of HAB for both LAS measurement and CFD simulation, and this can be attributed to the enhanced radiative heat loss to the surroundings. The CO₂ concentration remains almost unchanged at the HAB from 5 to 13 mm. The average central temperature difference between LAS measurement and CFD simulation is found to be within 20.0 K (< 1.1% relative) and the CO₂ concentration difference is within 700 ppm (< 1.0% relative). On the other hand, as shown by the open symbols, due to the discrepancy observed in the thermal boundary layer shown in Fig. 10, much larger discrepancies in the LOS-averaged temperature and concentration are observed between the LAS measurement and CFD.

5.4 LAS under optically thick conditions

Optically thick conditions (optical density > 1.0) are usually associated with high absorber number density, long optical pathlength and strong absorption linestrength [55, 56]. While increasing demands for highly sensitive measurements in real-field combustion environments have led to a pressing need for mid-IR absorption sensors, this essentially reduces the dynamic range of the transmission signal, with the upper limits of absorbance constrained by optically opaque conditions at the strong transition peaks. As illustrated in Fig. 4, even at a relatively short pathlength associated with the benchtop optical setup, CO₂ absorption in the fundamental band can be optically thick. Due to the large absorbance of the two low- E'' lines ($R(44)$, $R(46)$), pronounced mixing and interaction of hot CO₂ to the ambient surroundings near the flame boundary region can lead to further enhanced saturation in absorption. In addition, ambient CO₂ interference is unavoidable and the path-integrated absorption readily saturates.

Figure 12a shows a single-scan raw transmitted signal (black solid line) at HAB of 5 mm, $\varphi = 1.0$, and a measurement pathlength of ~53 cm. The instantaneous transmitted intensity reaches optically thick condition due to increased optical pathlength (from 28 to 53 cm) and flame instabilities even with the relatively stable McKenna burner. The transmission path becomes opaque with transmitted intensity reaching zero within random noise bounds at the two CO₂ fundamental transition peaks, as shown in the enlarged insets of Fig. 12a. This renders non-physical values of absorbance near the absorption line peaks, but with appropriate spectral reduction algorithm the integrated absorbance area for each absorption transition can still be estimated from evaluation of the absorption profile wings. To further extend the applicability of the developed sensing strategy to more practical combustion studies, data reduction schemes for LAS measurement under optically thick conditions is discussed in the following. Figure 12b presents the measured absorbance profile derived from Fig. 12a, together with non-linear least-square fits to the truncated lineshape region. The relative residuals are within 2.0% and is on similar level with the full absorbance profile fit in Fig. 12a. As such, the CO₂ absorption sensor developed here could be further extended to more practical combustion studies, e.g., in open long-path environments with ambient interference. However, the level of saturation in absorption will affect the accuracy of the proposed spectrum reduction algorithm, as only incomplete spectral profiles are used for Voigt fit. This effect becomes more pronounced especially with blended absorption features, as illustrated in Fig. 12a, but is not the main focus of this work. In conclusion, the developed data processing approach allows implementation in other measurement scenarios, where large dynamic range in the targeted measurand

Fig. 12 **a** Instantaneous measured CO₂ absorption raw signal at $\varphi = 1.0$ and HAB = 5 mm under optically thick condition, **b** Typical modified absorbance profile of CO₂ at $T = 1553$ K, $X_{\text{CO}_2} = 6.0\%$



is desired. Further demonstration is underway to investigate the performance of this mid-IR CO₂ sensor in more practical and harsh combustion environments.

6 Conclusions

A mid-IR CO₂ sensor with blended absorption features for non-uniform temperature and concentration of laminar premixed flame is developed. In general, precise LAS sensors desire selection of well-isolated absorption lines that are preferably free from blended hot bands. However, in complicated, practical combustion environments, the target absorption feature is usually inevitably spoiled by blended spectral features, ambient interference or optically thick conditions. Moreover, traditional two-line absorption thermometry provides LOS-averaged gas property measurements. Therefore, more accurate and quantitative spatially-resolved temperature or species concentration distribution measurement with single-LOS, multi-line absorption spectroscopy, can contribute to deeper understanding of complex combustion environments, and is still pressingly pursued.

The mid-IR CO₂ sensor presented here exhibits several important characteristics compared with previous LAS sensors: (1) The blended CO₂ absorption spectra with ambient self-interference can be well interpreted using IFBTBS method in high-temperature combustion environments. This is not only important for the extreme conditions associated with combustion, but also useful for exploiting novel laser sources with large spectral bandwidth for combustion-related spectroscopic studies; (2) The single-beam, multi-line absorption thermometry harnessing both molecular

fundamental and hot bands, opens up new opportunity to retrieve spatially-resolved gas property distributions along the laser beam path with a single laser. This would further simplify the design of the absorption sensor and optical configuration in LAS measurements, making it preferable for complicated sensing needs. However, it is worth noting that the sensor developed here aims at a more challenging and difficult situation, where ambient CO₂, blended absorption spectra both exist. This is the first time, to the best of our knowledge, that a CO₂ absorption sensor near 2380 cm⁻¹ targeting a group of blended hot band lines and strongly interfering ambient lines is developed. The demonstrated methodology in this work can be extended to different target mixtures using different portions of the spectra.

CO₂ absorption sensor covering eight absorption transitions between 2377.2 and 2379.0 cm⁻¹ is demonstrated in a laminar premixed CH₄/Air flat flame at $\varphi = 1.0$. Two cases are demonstrated, i.e., Case 1, absorption thermometry with 8 lines; Case 2, absorption thermometry with 2 lines ($R(44)$: $E_w'' = 772.1$ cm⁻¹ and $R(77)$: 3008.7 cm⁻¹), to further investigate the advantage of multi-line thermometry over conventional two-line thermometry under uniform and non-uniform conditions. It is shown that the LOS-averaged temperature can be determined with a precision of 24.0 K and the uncertainty of CO₂ concentration measurement is 0.21% in Case 1. The average signal-to-noise ratio is 1293 at a measurement time of 1.0 s, and the detection limit for CO₂ is estimated to be 42.8 ppm at 1543 K with 6 cm pathlength. The results show that under uniform conditions, multi-line thermometry (8 lines) outperforms conventional two-line thermometry in both measured uncertainty and relative residual. CFD simulation with reduced GRI 1.2 mechanism

is performed for comparison. The CFD simulation for central flame zone temperature and CO₂ concentration are in good agreement with the LAS measurement in two cases. Moreover, with multiple absorption lines in the non-uniform reconstruction, the radial position of boundary layer can be captured more accurately than that with only two lines selected at HAB = 9 mm. Difference between the LAS measurement and CFD simulation is found to be within 20.0 K (< 1.1% relative) for temperature and 700 ppm (< 1.0% relative) for CO₂ concentration. Small discrepancy is observed near the flame boundary region due to pronounced mixing and interaction of hot CO₂ with the ambient surroundings.

The novelties of this work are highlighted as follows: (1) A new CO₂ absorption sensor near 2380 cm⁻¹ is developed, with strong line strength and high temperature sensitivity, and free of spectral interference from H₂O and CO; (2) A new algorithm for interpreting absorption spectra with significantly blended features is proposed, combining IFBTBS method and single-line-of-sight multi-transition absorption thermometry at high-temperature combustion environments. In addition, the sum of the two merged transitions is treated effectively as a combined transition with a weighted line-strength $S_w(T)$ and lower-state energy E_w'' . This opens up new opportunity for LAS sensor design with more flexible absorption line selection; (3) Spatially-resolved temperature and CO₂ concentration distributions of CH₄/Air premixed flame is investigated, involving demonstrations from both LAS measurement and CFD simulation. The sensor developed here can serve to guide more general LAS sensor design with blended absorption features, ambient interference, or under optically thick conditions, and can be useful for various practical combustion studies (shock tube flows, practical combustor flames, etc.).

Acknowledgements National Natural Science Foundation of China (51976105, 91841302, 61627804); National Basic Research Program of China (JCKY2019204B020).

References

- R.K. Hanson, Proc. Combust. Inst. **33**(1), 1–40 (2011)
- X. Chao, Ph.D. Thesis, Stanford University (2012)
- M.A. Bolshov, Y.A. Kuritsyn, Y.V. Romanovskii, Spectrochim. Acta B: Atom. Spectrosc. **106**, 45–66 (2015)
- C.S. Goldenstein, R.M. Spearrin, J.B. Jeffries, R.K. Hanson, Prog. Energy Combust. Sci. **60**, 132–176 (2017)
- Z. Du, S. Zhang, J. Li, N. Gao, K. Tong, Appl. Sci. **9**(2), 338 (2019)
- C. Liu, L. Xu, Appl. Spectrosc. Rev. **54**(1), 1–44 (2019)
- Z. Wang, P. Fu, X. Chao, Appl. Sci. **9**(13), 2723 (2019)
- Z. Wang, P. Fu, X. Chao, Meas. Sci. Technol. **31**(3), 35202 (2019)
- K. Sun, X. Chao, R. Sur, C.S. Goldenstein, J.B. Jeffries, R.K. Hanson, Meas. Sci. Technol. **24**(12), 125203 (2013)
- A. Upadhyay, A.L. Chakraborty, Opt. Lett. **40**(17), 4086–4089 (2015)
- X. Liu, J.B. Jeffries, R.K. Hanson, AIAA J. **45**(2), 411–419 (2007)
- L. Ma, L.Y. Lau, W. Ren, Appl. Phys. B **123**(3), 83 (2017)
- L. Ma, K.-P. Cheong, H. Ning, W. Ren, Exp. Therm. Fluid Sci. **112**, 110013 (2020)
- K.-P. Cheong, L. Ma, Z. Wang, W. Ren, Appl. Spectrosc. **73**(5), 529–539 (2019)
- D. Wen, Y. Wang, Opt. Express **28**(25), 37879–37902 (2020)
- W. Cai, C.F. Kaminski, Prog. Energy Combust. Sci. **59**, 1–31 (2017)
- L. Ma, W. Cai, A.W. Caswell, T. Kraetschmer, S.T. Sanders, S. Roy, J.R. Gord, Opt. Express **17**(10), 8602–8613 (2009)
- N.A. Malarich, G.B. Rieker, J. Quant. Spectrosc. Radiat. Transf. **260**, 107455 (2021)
- N.A. Malarich, G.B. Rieker, J. Quant. Spectrosc. Radiat. Transf. **272**, 107805 (2021)
- C. Liu, L. Xu, Z. Cao, H. McCann, IEEE Trans. Instrum. Meas. **63**, 3067–3075 (2014)
- C. Liu, Z. Cao, F. Li, Y. Lin, L. Xu, Meas. Sci. Technol. **28**, 054002 (2017)
- A. Guha, I. Schoegl, J. Popul. Power. **53**, 350–359 (2014)
- A. Guha, I. Schoegl, Appl. Opt. **53**, 8095–8103 (2014)
- R.M. Mihalcea, D.S. Baer, R.K. Hanson, Meas. Sci. Technol. **9**(3), 327 (1998)
- R.M. Mihalcea, D.S. Baer, R.K. Hanson, Appl. Opt. **37**(36), 8341–8347 (1998)
- A. Farooq, J.B. Jeffries, R.K. Hanson, Appl. Phys. B **90**(3–4), 619–628 (2008)
- R.M. Spearrin, W. Ren, J.B. Jeffries, R.K. Hanson, Appl. Phys. B **116**(4), 855–865 (2014)
- K. Wu, F. Li, X. Cheng, Y. Yong, X. Lin, Y. Xia, Appl. Phys. B **117**(2), 659–666 (2014)
- J.J. Girard, R.M. Spearrin, C.S. Goldenstein, R.K. Hanson, Combust. Flame **178**, 158–167 (2017)
- X. Liu, G. Zhang, Y. Huang, Y. Wang, F. Qi, Appl. Phys. B **124**(4), 61 (2018)
- G. Zhang, G. Wang, Y. Huang, Y. Wang, X. Liu, Optik **170**, 166–177 (2018)
- T.W. Hänsch, Rev. Mod. Phys. **78**(4), 1297 (2006)
- N. Picqué, T.W. Hänsch, Nat. Photonics **13**(3), 146–157 (2019)
- Z. Wang, Z. Chen, X. Chao, E. Vicentini, T.W. Hänsch, N. Picqué, Front. Opt. Opt. Soc. Am. FW7B (2020). <https://doi.org/10.1364/FIO.2020.FW7B.3>
- F. Adler, P. Masłowski, A.A. Foltynowicz, K.C. Cossel, T.C. Briles, I. Hartl, J. Ye, Opt. Express **18**(21), 21861–21872 (2010)
- A.D. Draper, R.K. Cole, A.S. Makowiecki, J. Mohr, A. Zdanowicz, A. Marchese, N. Hoghooghi, G.B. Rieker, Opt. Express **27**, 10814–10825 (2019)
- L.A. Kranendonk, X. An, A.W. Caswell, R.E. Herold, S.T. Sanders, R. Huber, J.G. Fujimoto, Y. Okura, Y. Urata, Opt. Express **15**(23), 15115–15128 (2007)
- S.T. Sanders, Appl. Phys. B **75**(6), 799–802 (2002)
- M.C. Phillips, B.E. Bernacki, S.S. Harilal, J.M. Schwallier, N.G. Glumac, J. Appl. Phys. **126**(9), 093102 (2009)
- M.C. Phillips, T.L. Myers, T.J. Johnson, D.R. Weise, Opt. Express **28**(6), 8680–8700 (2020)
- M. Frenklach, H. Wang, C.-L. Yu, M. Goldenberg, C.T. Bowman, R.K. Hanson, D.F. Davidson, E.J. Chang, G.P. Smith, D.M. Golden, W.C. Gardiner, V. Lissianski, http://www.me.berkeley.edu/gri_mech/. (2021)
- X. An, A.W. Caswell, J.J. Lipor, S.T. Sander, J. Quant. Spectrosc. Radiat. Transf. **112**(14), 2355–2362 (2011)
- X. An, A.W. Caswell, S.T. Sanders, J. Quant. Spectrosc. Radiat. Transf. **112**(5), 779–785 (2011)
- S.T. Sanders, J. Wang, J.B. Jeffries, R.K. Hanson, Appl. Opt. **40**(24), 4404–4415 (2001)
- C. Liu, L. Xu, Z. Cao, Appl. Opt. **52**(20), 4827–4842 (2013)

46. V.V. Liger, V.R. Mironenko, Y.A. Kuritsyn, M.A. Bolshov, *Sensors* **18**(5), 1608 (2018)
47. N.A. Malarich, G.B. Rieker, *Laser Appl Chem Secur Environ Anal Opt Soc Am LW2C-6* (2018). <https://doi.org/10.1364/LAC-SEA.2018.LW2C.6>
48. S. Prucker, W. Meier, W. Stricker, *Rev. Sci. Instrum.* **65**(9), 2908–2911 (1994)
49. Z. Qu, O. Werhahn, V. Ebert, *Appl. Spectrosc.* **72**(6), 853–862 (2018)
50. L.S. Rothman, I.E. Gordon, R.J. Barber, H. Dothe, R.R. Gamache, A. Goldman, V.I. Perevalov, S.A. Tashkun, J. Tennyson, *J. Quant. Spectrosc. Radiat. Transf.* **111**(15), 2139–2150 (2010)
51. C.S. Goldenstein, V.A. Miller, R.M. Spearrin, C.L. Strand, J. *Quant. Spectrosc. Radiat. Transf.* **200**, 249–257 (2017)
52. B.C. Reed, *Am. J. Phys.* **57**(7), 642–646 (1989)
53. K. Shojaei, 17th Mediterranean conference on control and automation. IEEE, pp. 1050–1055 (2009)
54. W. Ben-Ameur, *Comput. Optim. Appl.* **29**(3), 369–385 (2004)
55. Z. Qu, E. Steinvall, R. Ghorbani, F.M. Schmidt, *Anal. Chem.* **88**(7), 3754–3760 (2016)
56. E. Thorin, F.M. Schmidt, *Opt. Lett.* **45**(18), 5230–5233 (2020)

Publisher's Note Springer Nature remains neutral with regard to jurisdictional claims in published maps and institutional affiliations.